Journal of Alloys and Compounds 509 (2011) 6578–6584

Contents lists available at ScienceDirect

Journal of Alloys and Compounds

journal homepage: www.elsevier.com/locate/jallcom

Polarized spectral analysis of Er^{3+} ions in Er^{3+}:$LiGd(MoO_4)_2$ crystal

Xinyang Huang[a,*], Wang Zhao[b], Guofu Wang[c], Xiaoxia Li[a], Quanmao Yu[a]

[a] Institute of Research on the Functional Matter, Jiangxi University of Finance and Economy, Nanchang Jiangxi 330013, PR China
[b] Department of Physics, Huainan Normal University, Huainan, Anhui 232001, PR China
[c] Institute of Research on the Structure of Matter, Chinese Academy of Sciences, Fuzhou, Fujian 350002, PR China

ARTICLE INFO

Article history:
Received 10 May 2010
Received in revised form 5 March 2011
Accepted 8 March 2011
Available online 16 March 2011

Keywords:
Er^{3+}:$LiGd(MoO_4)_2$ crystal
Spectroscopic characteristics
Upconversion

ABSTRACT

The Er^{3+}:$LiGd(MoO_4)_2$ crystal with Ø21 × 33 mm^3 was grown by the Czochralski technique, and the absorption spectra, the fluorescence spectra and the fluorescence decay curves were measured at room temperature. Some spectroscopic parameters, such as the parameters of oscillator strengths, the spontaneous transition probabilities, the fluorescence branching ratios, the radiative lifetimes and the emission cross-sections were estimated based on Judd–Ofelt theory and Füchtbauer–Ladenburg method. The infrared emission at 1450–1650 nm, due to $^4I_{13/2} \rightarrow {}^4I_{15/2}$ transition and the visible emission at 520–569 nm corresponding to $^2H_{11/2}, {}^4S_{3/2} \rightarrow {}^4I_{15/2}$ transition were observed in Er^{3+}:$LiGd(MoO_4)_2$ crystals under 979 nm excitation at room temperature. The emission cross-sections are 4.37×10^{-20} cm^2 at 553 nm and 0.584×10^{-20} cm^2 at 1561 nm for π-polarization, and the following measured lifetimes are 4.57 ms and 10.74 μs. The upconversion emissions were attributed to energy transfer between Er^{3+} ions and the excited state absorption.

1. Introduction

The development of the compact eye-safe and visible-wavelength Er^{3+} lasers has been a subject of numerous studies. The infrared emission around 1.55 μm of Er^{3+}, located in the optical communication window, is used in medicine, optics communication and ranging (LIDAR), and 0.55 μm laser is used in various fields, such as data storage, submarine communication and laser display. Er^{3+} ion has a favorable energy-level structure with $^4I_{15/2} \rightarrow {}^4I_{9/2}$ transition (≈800 nm) and $^4I_{15/2} \rightarrow {}^4I_{11/2}$ transition (≈970 nm) in the near-infrared spectral region, which allows the pumping with commercial high power semiconductor lasers. Therefore, the Er^{3+}-doped bulk crystals, nano-/micro-materials and glasses have attracted more and more interest [1–13].

The double molybdate crystals with the formula $MRe(MoO_4)_2$ (M = alkali metal, Re = rare earth) as host materials for solid-state lasers have widely been investigated and possess the durability in the air atmosphere, large nonlinear optical susceptibility χ^3 (leading to be efficient Raman shifter), and large lanthanide ion acceptance [9–22]. The $LiGd(MoO_4)_2$ (LGM) crystal, one member of the $MRe(MoO_4)_2$, belongs to the tetragonal system with the scheelite crystal structure [21]. The $LiGd(MoO_4)_2$ crystal can be regarded as a disordered structure because Li^+ and Gd^{3+} are distributed randomly, and this disordered structure usually makes the rare earth doped have broad absorption and emission band [11,22]. The $LiGd(MoO_4)_2$ crystal melts congruently and has no polymorphic transformation from its melting point to room temperature, thus, rare-earth doped $LiGd(MoO_4)_2$ crystal can be grown by Czochralski method. Green and red upconversion emission in Er^{3+}/Yb^{3+}-codoped $LiGd(MoO_4)_2$ crystal was observed under 976 nm excitation [11]. However, the thermal expansion coefficient parallel and perpendicular to the optical axis differs approximately by two times, that is to say, the $LiGd(MoO_4)_2$ crystal has large thermal expansion anisotropy, thereby, there exist many minute cracks in the as-grown Er^{3+}/Yb^{3+}-codoped $LiGd(MoO_4)_2$ crystal (see Fig. 1 in Ref. [11]) and the scattering phenomena were observed under the irradiation of xenon lamp, which may be resulted from structural defects (stacking faults, dislocations, point defect complexes, and others) [23]; some optical parameters of Er^{3+}:$LiGd(MoO_4)_2$ crystal, such as the fluorescence lifetime, the absorption and emission cross sections have not been reported. These may limit the further study of the Er^{3+}:$LiGd(MoO_4)_2$ crystal laser. Therefore, the main objective of this paper is to investigate the spectroscopic properties of Er^{3+}:$LiGd(MoO_4)_2$ crystal.

2. Experimental details

To obtain one Er^{3+}:$LiGd(MoO_4)_2$ crystal with high quality, non-scattering and micro-cracks free, some growth technology was explored on basis of the growth procedure described in Ref. [11] and [22]. The Pt plate was placed in the top of the hot insulation and the thickness of the insulation was added to decrease the temperature gradient; the pulling rate was decreased to 0.3–0.5 mm/h and the rotation rate was increased to 60–80 r/m during the growth process; and the crystal was cooled down to room temperature at a small rate (10–20 °C/h) after the growth ended. As

* Corresponding author. Tel.: +86 791 3891364; Fax: +86 791 3891364.
E-mail address: xyhang0202@hotmail.com (X. Huang).

0925-8388/$ – see front matter © 2011 Elsevier B.V. All rights reserved.
doi:10.1016/j.jallcom.2011.03.061

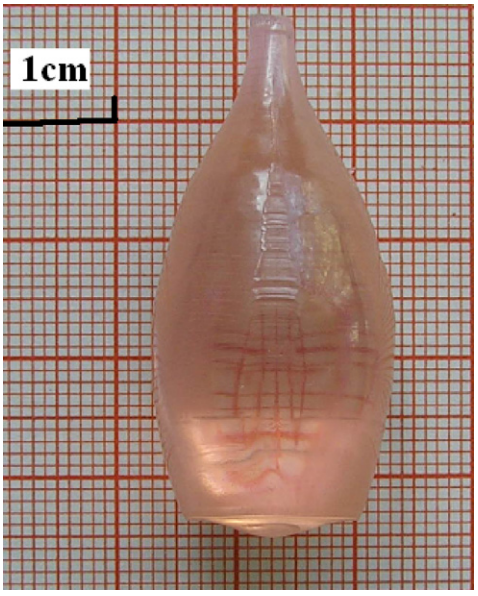

Fig. 1. The photo of the as-grown Er^{3+}:$LiGd(MoO_4)_2$ crystal by Czochralski technique.

a result, the 5.0 at.% Er^{3+}:$LiGd(MoO_4)_2$ crystal with Ø21 × 33 mm^3 and pink color was obtained, as shown in Fig. 1. In the as-grown Er^{3+}:$LiGd(MoO_4)_2$ crystal there exists no minute crack and the scattering light was not observed under the irradiation of xenon lamp. Other Er^{3+}:$LiGd(MoO_4)_2$ crystals with different initial melt concentrations (0.5 at.%, 1.0 at.%, and 3.0 at.%) were also grown in the same way.

The crystal orientation was determined by the Laue technique using an YX-2 type Orientation Unit. The investigated samples were cut into the dimension of 5.0 × 5.0 × 2.0 mm^3, polished and applied for the spectroscopic experiments. The 5 mm × 5 mm facet is parallel to the *c*-axis. According to the tetragonal character of the lattices, the experimental spectra are labeled as σ or π, which are defined in term of the **E**-vector being perpendicular and parallel to the optical axis *c*, respectively.

The X-ray powder diffraction (XRD) patterns were collected using a D/max-rA diffractometer and employing CuKα radiation (λ = 1.54056 Å) at room temperature. The samples cut from the top, middle and bottom of the as-grown crystals were applied to measure Er^{3+} concentrations in as-grown crystals using the inductively coupled plasma and atomic emission spectrometry (ICP-AES) technique.

The room temperature polarized absorption spectra were measured using a Perkin-Elmer UV-VIS-NIR spectrometer (Lamada-900) in the range of 300–1700 nm. The emission spectra and the fluorescence decay curves were preformed using the Edinburgh Analysis Instruments FLS920 spectrophotometer with laser-diode (LD) and xenon lamp as pumping sources, and the following excitation wavelengths were 979 nm and 488 nm. The fluorescence decay curves at 1561, 1000 and 553 nm, corresponding to $^4I_{13/2} \rightarrow {}^4I_{15/2}$, $^4I_{11/2} \rightarrow {}^4I_{15/2}$, and $^4S_{3/2} \rightarrow {}^4I_{15/2}$ transitions, respectively, were measured at room temperature.

3. Result and discussion

3.1. Doped concentration and phase structure

The measured Er^{3+} concentration in the top, middle and bottom of the Er^{3+}:$LiGd(MoO_4)_2$ crystals (see Table 1) is close to the Er^{3+} concentration in the respective initial melt, implying that Er^{3+} ions are distributed uniformly in $LiGd(MoO_4)_2$ crystal. This Er^{3+} uniformly distribution phenomenon along the Er^{3+}:$LiGd(MoO_4)_2$ crystal is similar to that along the Er^{3+}:Yb^{3+}:$LiGd(MoO_4)_2$ crystal [11].

The pattern of X-ray power diffraction (XRD) of as-grown Er^{3+}:$LiGd(MoO_4)_2$ crystal at room temperature was shown in Fig. 2. Compared with the Joint Committee on Powder Diffraction Standard (JCPDS) card No:023-1179) [24], the as-grown Er^{3+}:$LiGd(MoO_4)_2$ crystal had some split XRD peaks and the distorted shapes of the as-grown Er^{3+}:$LiGd(MoO_4)_2$ crystal were observed. This could be resulted from the formation of ordered phase with lowering of the crystal symmetry and the formation of the super-structure [23,25–27]. X-ray diffraction analysis by using

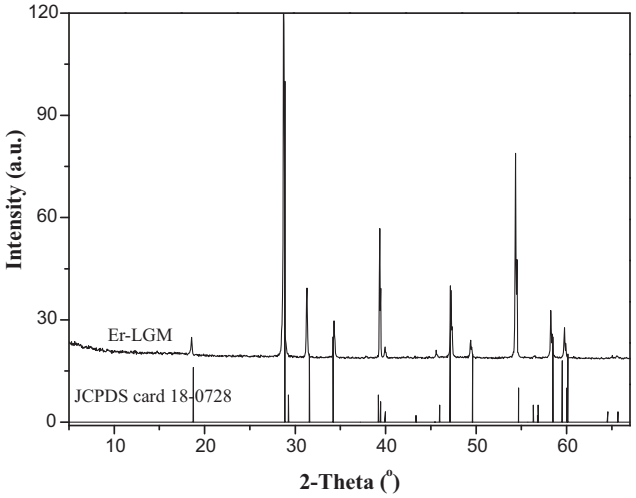

Fig. 2. The XRD pattern of Er^{3+}:$LiGd(MoO_4)_2$ crystal and the standard data (JSPDS card no. 18-0728) as a reference.

Topas 2 program shows that the as-grown Er^{3+}:$LiGd(MoO_4)_2$ crystal belongs to tetragonal system with I-4 space group and unit cell parameters: a_0 = 10.353 Å, c_0 = 22.471 Å.

3.2. Polarized absorption spectra and analysis

The room-temperature polarized absorption spectra of 4.84 at.% Er^{3+}:$LiGd(MoO_4)_2$ crystal were depicted in Fig. 3. The spectra are typical for Er^{3+} in crystals, and the groups of the lines near 407, 451, 488, 522, 553, 653, 801, 982 and 1536 nm are originated from the $^4I_{15/2}$ ground state to the $^2H_{9/2}$, $^4F_{5/2}$ + $^4F_{3/2}$, $^2H_{11/2}$, $^4S_{3/2}$, $^4F_{9/2}$, $^4I_{7/2}$, $^4I_{9/2}$, $^4I_{11/2}$ and $^4I_{13/2}$ of Er^{3+} according to the prominent literature on the absorption features in Er^{3+}-doped crystals and glasses [1]. To our interest, for π-polarization, the peak absorption wavelength of the $^4I_{15/2} \rightarrow {}^4I_{11/2}$ is located at 979 nm, whereas for σ-polarization, this wavelength shifts to 982 nm, and the peak absorption coefficient for π- polarization is close to that for σ-polarization, while the peak absorption wavelength of the $^4I_{15/2} \rightarrow {}^4I_{9/2}$ lies at 801 nm for π- and σ- polarization, and the peak absorption coefficient for π-polarization is about 2 times larger than that for σ-polarization. Thereby, the pumping wavelength was chose to 979 nm. The corresponding absorption cross section σ_{abs} was determined by $\sigma_{abs} = \alpha/\rho$ with α being the absorp-

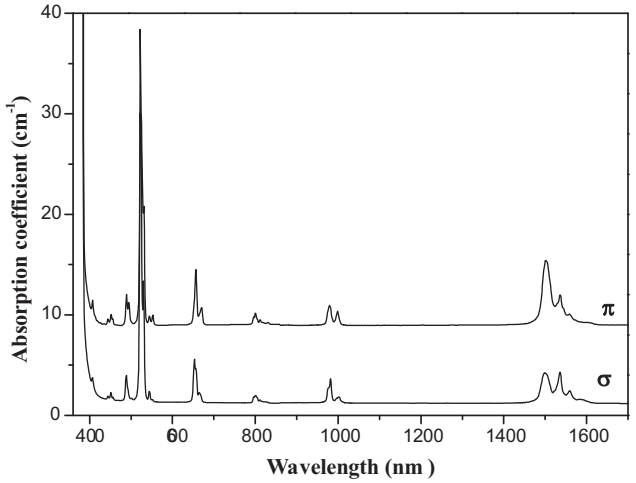

Fig. 3. Polarized absorption spectra of Er^{3+}:$LiGd(MoO_4)_2$ crystal at room temperature.

Table 1
The measured Er^{3+} concentration in the as-grown Er^{3+}:$LiGd(MoO_4)_2$ crystals and the Er^{3+} concentration in the initial melt.

Sample	The concentration in the initial melt (at.%)	The concentration in as-grown crystals (at.%)		
		Top	Middle	Bottom
1#	0.5	0.58	0.55	0.53
2#	1.0	1.15	1.09	1.04
3#	3.0	2.79	2.84	2.87
4#	5.0	4.69	4.79	4.85

Table 2
The absorption cross section at 804 and 982 nm in Er^{3+}:$LiGd(MoO_4)_2$ crystal.

	σ-polarization		π-polarization	
Wavelength (nm)	801	982	801	979
Absorption cross section (10^{-20} cm^2)	0.25	0.83	0.42	0.69

tion coefficient and ρ being the Er^{3+} concentration, as shown in Table 2. The value of absorption cross section of Er^{3+}:$LiGd(MoO_4)_2$ crystal near 980 nm is similar to that of Er^{3+}:$NaGd(WO_4)_2$ [13], Er^{3+}:$NaY(MoO_4)_2$ [14], and Er^{3+}:$LiLa(MoO_4)_2$ crystals [19], indicating the Er^{3+}:$LiGd(MoO_4)_2$ crystal has a strong absorption capability of the pumping light.

Based on Judd–Ofelt theory [29,30], the data of seven absorption bands were used to predict the parameters of oscillator strengths Ω_λ (λ = 2, 4 and 6), the radiative lifetimes τ_{rad}, the transition probabilities A_{rad} and the fluorescence branching ratios β. The detailed procedure was given in the previous works [13]. Since the magnetic dipole has a significant contribution to the $^4I_{15/2} \rightarrow {}^4I_{13/2}$ transition, the magnetic dipole line strength was subtracted from the experimental line strength value [1,31]. The $^4I_{15/2} \rightarrow {}^2H_{11/2}$ transition was excluded due to its hypersensitive nature [31]. The $^4I_{15/2} \rightarrow {}^4S_{3/2}$ transition was also excluded since it overlapped the $^4I_{15/2} \rightarrow {}^2H_{11/2}$ transition. The refractive index of $LiGd(MoO_4)_2$ crystal is 1.95 [21], and $\left\langle \|U^{(\lambda)}\| \right\rangle$ the double reduce matrix elements of the unit tensor operators are in Ref. [1] and [31].

The relation between the polarized and effective parameters of oscillator strengths for the uniaxial crystal can be generally defined as $\Omega_{eff} = (2\Omega_\pi + \Omega_\sigma)/3$. The results obtained (see Table 3) show that the Ω_2 values of Er^{3+}:$LiGd(MoO_4)_2$ crystal are very large and close to that of other Er^{3+}-doped disorder scheelite crystals (see Table 3 in Ref. [19]), indicating that this crystal exhibit strong covalency of Er–O bond..

Once the effective parameters of oscillator strengths were obtained, the calculated line strengths S_{cal} of Er^{3+} in Er^{3+}:$LiGd(MoO_4)_2$ were listed in Table 4 with the mean wavelength and the experimental line strengths S_{ed}. The transition probabilities ($A_{JJ'}$), fluorescence branching ratios ($\beta_{JJ'}$) and radiative lifetimes (τ_r) for main Er^{3+} multiplets were summarized in Table 5.

3.3. Emission spectra and stimulated emission cross-sections

The polarized emission spectra of 4.84 at.% Er^{3+}:$LiGd(MoO_4)_2$ crystal at room temperature were shown in Fig. 4a. The excited wavelength used was 979 nm. The intensity at 1400–1650 nm attributed to $^4I_{13/2} \rightarrow {}^4I_{15/2}$ transition is much larger than that at 940–1040 nm due to $^4I_{11/2} \rightarrow {}^4I_{15/2}$ transition and the intensity of the former is as 3–8 times as that of the latter. The emission band at 1485–1650 nm consists of many sharp peaks, and the intensity for π-polarization is about 3 times stronger than that for σ-polarization. The emission band near 1550 nm has a full width at half-maximum (FWHM) of about 113 nm. The value is close to that of Er^{3+}:$NaGd(WO_4)_2$ [13], Er^{3+}:$NaY(MoO_4)_2$ [14], and Er^{3+}:$LiLa(MoO_4)_2$ crystal [19], and larger than that of Er^{3+}:YAG [32], Er^{3+} doped ZBLAN glass [33] and Er^{3+}:Y_2O_3 [34]. Such an FWHM can probably be resulted from the disorder structure of $LiGd(MoO_4)_2$ crystal. This implies that the Er^{3+}:$LiGd(MoO_4)_2$ crystal may be regarded as a potential the generation of the tunable laser pulse near 1550 nm.

The emission cross-section σ_e of the main channel $^4I_{13/2} \rightarrow {}^4I_{15/2}$ can be derived using the Füchtbauer–Ladenburg equation [35,36]:

$$\sigma_e = \frac{3\lambda^5 I(\lambda)}{8c\pi\tau n^2 \int \lambda[I_\sigma(\lambda) + 2I_\pi(\lambda)]d\lambda} \quad (1)$$

where λ is the emission wavelength, τ is the radiative lifetime, which is 4.895 ms (see Table 4), and n is the refractive index which

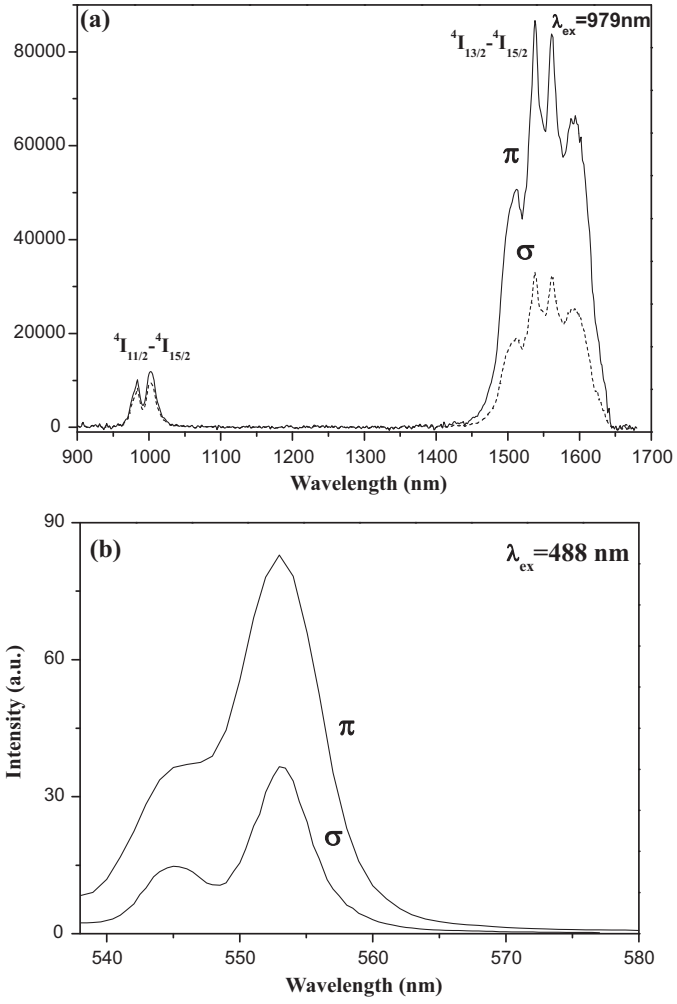

Fig. 4. Polarized fluorescence spectra of Er^{3+}: $LiGd(MoO_4)_2$ crystal excited with (a) 979 and (b) 488 nm LD at room temperature.

Table 3
The parameters of oscillator strengths of Er^{3+}:$LiGd(MoO_4)_2$ crystals.

	σ-polarization	π-polarization	Effective
$\Omega_2(10^{-20}\,cm^2)$	15.58	15.62	15.60
$\Omega_4(10^{-20}\,cm^2)$	2.52	2.09	2.23
$\Omega_6(10^{-20}\,cm^2)$	1.32	2.39	2.03
Ω_4/Ω_6	1.90	0.87	1.09

Table 4
Mean wavelength, the experimental and calculated line strengths S_{ed} of Er^{3+} in Er^{3+}:$LiGd(MoO_4)_2$ crystal.

Excited state (from $^4I_{15/2}$)	$\bar{\lambda}$ (nm)	$\int_{mean} k(\lambda)d\lambda$ (nm/cm)	S_{ed} ($10^{-20}\,cm^2$)	S_{cal} ($10^{-20}\,cm^2$)
$^4I_{13/2}$	1538	237.77	4.43	4.18
$^4I_{11/2}$	982	32.11	0.91	1.08
$^4I_{9/2}$	801	16.21	0.57	0.49
$^4F_{9/2}$	653	51.10	2.18	2.22
$^4F_{7/2}$	488	24.55	1.76	1.80
$^4F_{5/2} + {}^4F_{3/2}$	451	8.39	0.62	0.64
$^2H_{9/2}$	407	3.64	0.35	0.38
RMS		3.46%		

is 1.95, $I(\lambda)$ is the fluorescence intensity at wavelength λ. The peak emission cross sections obtained by using Eq. (1) are 0.584×10^{-20} and $0.224 \times 10^{-20}\,cm^2$ at 1568 nm for π- and σ-polarization, respectively. The values are close to these reported for other Er^{3+}-doped materials, such as $0.76 \times 10^{-20}\,cm^2$ (π) and $0.78 \times 10^{-20}\,cm^2$ (σ) for Er^{3+}:$NaGd(WO_4)_2$ [13], $0.78 \times 10^{-20}\,cm^2$ (π) and $1.1 \times 10^{-20}\,cm^2$ (σ) for Er^{3+}:$NaY(MoO_4)_2$ [14], $0.95 \times 10^{-20}\,cm^2$ (π) and $0.86 \times 10^{-20}\,cm^2$ (σ) for Ce^{3+},Er^{3+}:$NaLa(MoO_4)_2$ [28], and $0.45 \times 10^{-20}\,cm^2$ for Er^{3+}:YAG [32], which is advantageous for the generation of laser operation.

The room temperature emission spectra in the region of 500–750 nm were obtained under 488 nm excitation and shown in Fig. 4b. Green light emission was observed between 520 and 560 nm due to $^2H_{11/2}$,$^4S_{3/2} \rightarrow {}^4I_{15/2}$ transition of Er^{3+}, and the emission after 560 nm is too weak to be detected in current experiment condition. And the emission cross sections obtained using Eq. (1)

Table 5
Spontaneous-emission probabilities, radiative branching ratios, radiative and measured lifetime (τ_R) of Er^{3+} in Er^{3+}:$LiGd(MoO_4)_2$ crystal at room temperature.

Manifold		λ (nm)	S_{cal} ($10^{-20}\,cm^2$)	A_{ed} (s^{-1})	A_{md} (s^{-1})	β (%)	τ_r (ms)	τ_f (ms)
$^4I_{13/2}\rightarrow$	$^4I_{15/2}$	1538.4	1.4267	123.08	81.2	100	4.895	4.57
$^4I_{11/2}\rightarrow$	$^4I_{13/2}$	2777.8	1.3154	24.39	17.8	7.01	1.721	0.115
	$^4I_{15/2}$	990.1	0.5412	538.7		92.99		
$^4I_{9/2}\rightarrow$	$^4I_{11/2}$	4651.2	0.1968	6.2	4.3	3.18	0.263	–
	$^4I_{13/2}$	1739.1	0.5873	119.3		8.35		
	$^4I_{15/2}$	800	0.1905	1225.5		88.79		
$^4F_{9/2}\rightarrow$	$^4I_{9/2}$	3508.8	1.0542	14.52		0.53	0.372	–
	$^4I_{11/2}$	1980.2	1.6034	80.8	3.5	3.13		
	$^4I_{13/2}$	1156.1	0.2997	406.1		15.02		
	$^4I_{15/2}$	660.1	0.9339	2182		80.73		
$^4S_{3/2}\rightarrow$	$^4F_{9/2}$	3125	0.0215	51.4		0.39	0.075	0.0107
	$^4I_{9/2}$	1639.3	0.2862	356.0		2.69		
	$^4I_{11/2}$	1212.1	0.0635	880.8		6.03		
	$^4I_{13/2}$	863.6	0.2769	2435.9		18.27		
	$^4I_{15/2}$	545	0.1769	9692.7		74.45		
$^2H_{11/2}\rightarrow$	$^4S_{3/2}$	12500	0.2176	0.27		0.005	0.188	–
	$^4F_{9/2}$	2500	2.9351	33.5		0.63		
	$^4I_{9/2}$	1449	1.9638	171.8		3.23		
	$^4I_{11/2}$	1105	0.4615	387.6		7.29		
	$^4I_{13/2}$	791	0.2934	1058.4		19.90		
	$^4I_{15/2}$	522	6.2214	3672		69.03		
$^4F_{7/2}\rightarrow$	$^2H_{11/2}$	8695	1.3229	1.1929		0.003	0.023	–
	$^4S_{3/2}$	5128	0.0069	5.8158		0.015		
	$^4F_{9/2}$	1923	0.1451	110.3		0.25		
	$^4I_{9/2}$	1242	0.5734	409191		94.11		
	$^4I_{11/2}$	980.4	0.4284	832.4		1.91		
	$^4I_{13/2}$	724.6	0.3554	2061.31		0.47		
	$^4I_{15/2}$	492.6	0.6560	6561.4		1.51		
$^4F_{5/2}\rightarrow$	$^4F_{7/2}$	6060.6	0.7476	4.7		0.023	0.055	-
	$^2H_{11/2}$	3571.4	0.2078	22.9		0.05		
	$^4S_{3/2}$	2777.8	0.0699	48.7		0.10		
	$^4F_{9/2}$	1459.9	0.5476	336.1		1.85		
	$^4I_{9/2}$	1030.9	0.2281	954.5		5.25		
	$^4I_{11/2}$	843.9	1054	1740.2		9.37		
	$^4I_{13/2}$	647.2	0.4623	3856.8		21.21		
	$^4I_{15/2}$	455.6	0.1786	11059		60.82		

are 4.37×10^{-20} and 1.93×10^{-20} cm^2 at 553 nm for π- and σ-polarization, respectively.

3.4. Fluorescence lifetime

The fluorescence decay curve at 1561 nm for Er^{3+}:$LiGd(MoO_4)_2$ crystal is shown in Fig. 5a. The lifetime τ_f of $^4I_{13/2}$ determined by the single exponential fitting is around 7.20 ms, which is longer than the radiative time (see Table 5). This phenomenon has also existed in some other Er^{3+}-doped hosts, such as Er^{3+}:$NaGd(WO_4)_2$ [13], Er^{3+}:$NaY(MoO_4)_2$ [14], and Er^{3+}:$LiLa(MoO_4)_2$ [19]. There exist energy transfer between Er^{3+}, the excited state absorption and serious self-absorption in Er^{3+}:$LiGd(MoO_4)_2$ crystal; therefore, the rate of the depopulation from $^4I_{13/2}$ decreases, accordingly, resulting in the increase of the measured lifetime of $^4I_{13/2}$ [35,36]. To minimize this phenomenon, the room temperature lifetime of the $^4I_{13/2}$ Er^{3+}multiplet was measured on Er^{3+}:$LiGd(MoO_4)_2$ powders dispersed in toluene. The toluene refractive index $n = 1.495$ decreases the fraction of emission trapped in the particles by the inner reflection. The fluorescence decay curve obtained (see Fig. 5a) was fitted by the single exponential with a time constant $\tau_f = 4.57$ ms, which is very close to the radiative time (see Table 5).

The fluorescence decay curve of the $^4S_{3/2}$ state, as shown in Fig. 5b, exhibits the single exponential, implying that there exist no additional processes. The fluorescence lifetimes of the $^4S_{3/2}$ state obtained is 10.74 μs. The quantum efficiency $\eta = \tau_{em}/\tau_{rad}$ with the radiative lifetime of 75 μs (see Table 5) is determined to be 14.32%. The Er^{3+}:$LiGd(MoO_4)_2$ crystal also exhibits large emission cross-sections and branching ratios of $^4S_{3/2} \rightarrow {}^4I_{15/2}$ transition, giving hope to obtain green upconversion lasing around 0.55 μm.

The fluorescence decay curve of the $^4I_{11/2}$ state is shown in Fig. 5c to evaluate the relaxation rate from the $^4I_{11/2}$ to the $^4I_{13/2}$ upper level. The measured lifetimes of bulk and powder crystals are about 115 μs, which indicates that the effect of re-absorption is weak for the emission from the transition of the $^4I_{11/2} \rightarrow {}^4I_{15/2}$. The lifetime is similar to that of Er^{3+}:YAG (100 μs) [37] but longer than those of Er^{3+}:$Ca_2Al_2SiO_7$ (41 μs) [38], and Er^{3+}:YVO_4 (23 μs) [39]. As to be discussed in Section 3.4, the longer fluorescence lifetime and higher quantum efficiency (6.68%) of $^4I_{11/2}$ in Er^{3+}:$LiGd(MoO_4)_2$ crystal are disadvantageous to the population in the upper laser level of $^4I_{13/2}$.

3.5. Upconversion fluorescence

When these crystals were excited with a LD of pump power about several mW under 979 nm excitation, the green upconversion emission was observed by naked eyes. The polarized upconversion fluorescence spectra were depicted in Fig. 6. The upconversion emission exhibits a strong dependence on the polarization and the intensity for π-polarization is much larger than that for σ-polarization. Strong upconversion emission bands attributed to the ($^2H_{11/2}$, $^4S_{3/2}$)$\rightarrow {}^4I_{15/2}$ transition of Er^{3+} ion were observed in the region of 512–573 nm. And the upconversion emission in the wavelength range of 560–800 nm was too weak to be observed. However, the red upconversion emission from $^4F_{9/2}$ in Er^{3+}/Yb^{3+}-codoped $LiGd(MoO_4)_2$ crystal was detected under 976 nm excitation [11]. The explanation was given in the following. Since the lifetime of $^4I_{11/2}$ state is very short, some ions in the $^4I_{11/2}$ state nonradiatively decay to $^4I_{13/2}$ state, and jump to $^4F_{9/2}$ state by the excited state absorption, the energy transfer from the $^4I_{11/2}$ state of an adjacent Er^{3+}, and the phonon assisted energy transfer from the excited state $^2F_{5/2}Yb^{3+}$. The Yb^{3+} ion has a larger absorption cross-section than the Er^{3+} ion around 976 nm, and the Yb^{3+} concentration is larger than that of Er^{3+} in Er^{3+}/Yb^{3+}-codoped $LiGd(MoO_4)_2$ crystal; thereby, the $^4F_{9/2}$ state Er^{3+} ions mostly originate from the phonon assisted energy transfer from the excited state $^2F_{5/2}Yb^{3+}$.

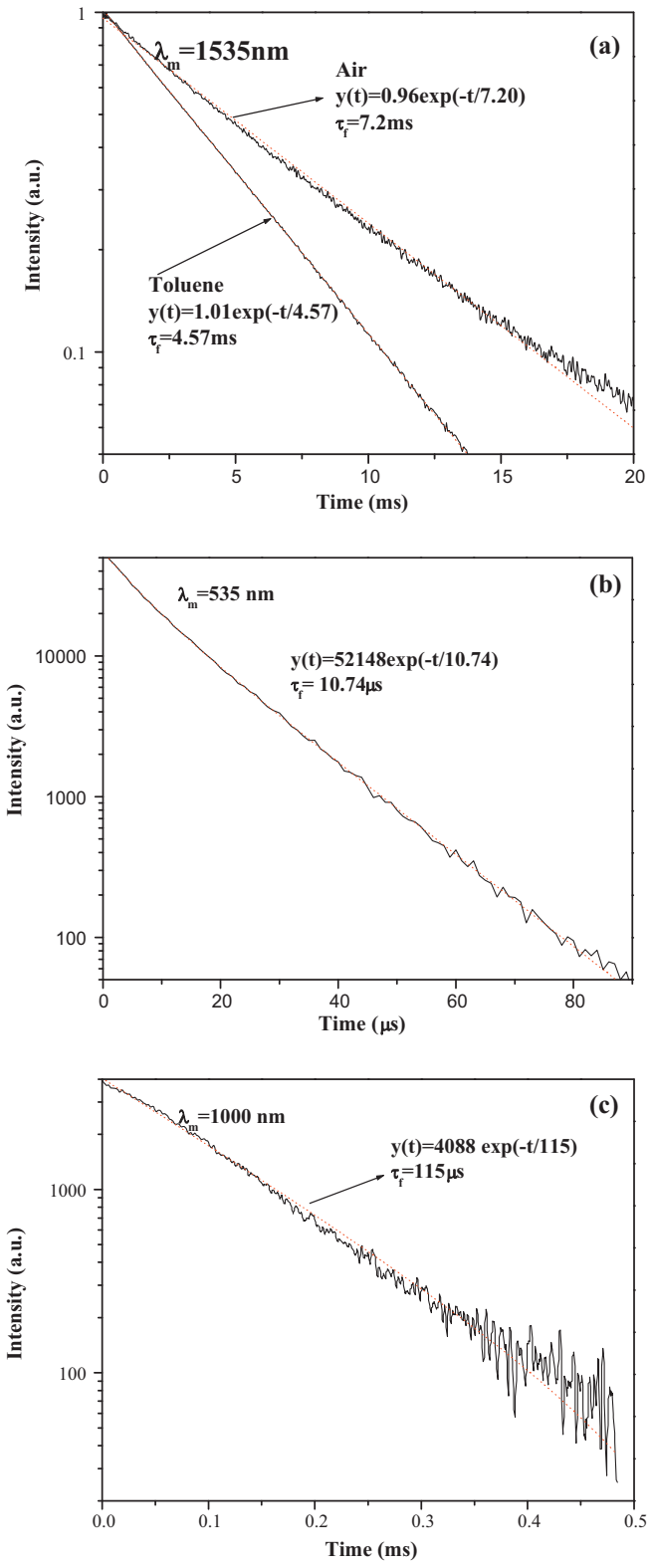

Fig. 5. Fluorescence decay curves at 535, 1000 and 1535 nm of Er^{3+}:$LiGd(MoO_4)_2$ crystal.

Fig. 7 shows the relationship between upconversion emission intensity of Er^{3+}:$LiGd(MoO_4)_2$ crystal for π-polarization under 979 nm excitation and different Er^{3+} concentrations. It can be seen that the emission intensities at 534, 545 and

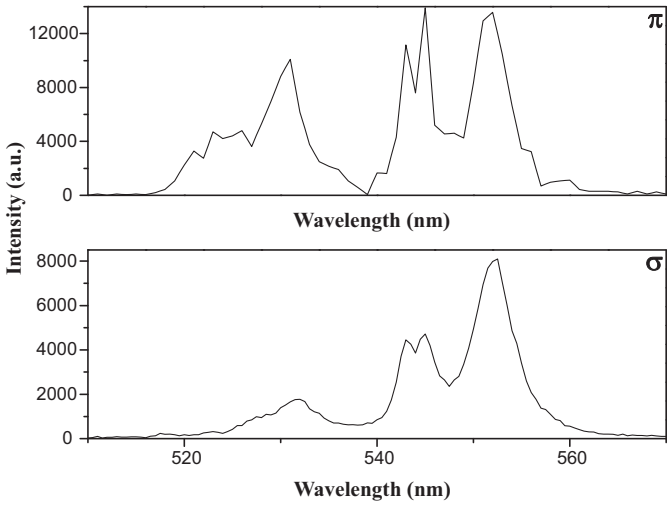

Fig. 6. Polarized upconversion emission spectra of Er^{3+}:LiGd$(MoO_4)_2$ crystal under 979 nm excitation at room temperature

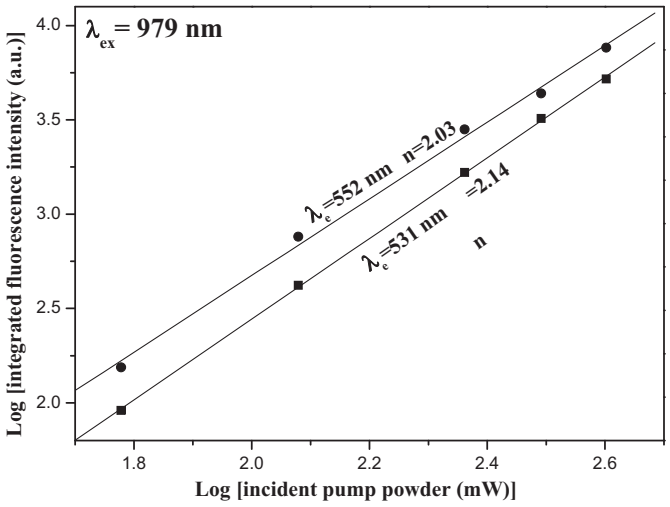

Fig. 8. Dependence of the upconversion fluorescence intensity on the incident pump power for the Er^{3+}:LiGd$(MoO_4)_2$ crystal under excitation at 979 nm.

553 nm become stronger and stronger with the increase of Er^{3+} concentration.

To understand the upconversion emission mechanism by which the ($^4S_{3/2}$,$^2H_{11/2}$) excited states were populated under 979 nm irradiation, the upconversion emission intensities of the green ($^4S_{3/2}$,$^2H_{11/2} \rightarrow {}^4I_{15/2}$) transitions were measured as a function of the excitation power (see Fig. 8). For upconversion mechanism, the visible output power intensity (I_v) is proportional to some power (n) of the infrared excitation intensity (I_{IR}): $I_v \infty I_{IR}^n$ with n being the number of IR photons absorbed per visible photon emitted. The slope for ($^4S_{3/2}$, $^2H_{11/2}$)$\rightarrow {}^4I_{15/2}$ is 2.05 under 979 nm excitation, indicating that two-photon processes were mainly involved in the upconversion mechanism responsible for populating the ($^2H_{11/2}$, $^4S_{3/2}$) levels.

To sum up, it is believed that the upconversion emission is resulted from the excited state absorption (EAS) or the energy transfer (ET) process between Er^{3+} ions in Er^{3+}:LiGd$(MoO_4)_2$ crystal. The upconversion emission process is as follows (see Fig. 9).

The 979 nm LD excites the $^4I_{15/2}$ ground state Er^{3+} ions to the $^4I_{11/2}$ excited state. One part of the excited state $^4I_{11/2}$ Er^{3+} ions depopulate to the $^4I_{15/2}$ ground state, producing the 970–1020 nm light, while another part energy transfers to the adjacent Er^{3+} in the ground state $^4I_{15/2}$, accordingly, also exciting it to the excited state $^4I_{11/2}$. This process can be described as:

$$^4I_{15/2}(Er^{3+}) + h\nu(979\,\text{nm}) \rightarrow {}^4I_{11/2}(Er^{3+})(\text{GSA})$$

$$^4I_{11/2}(Er1^{3+}) + {}^4I_{15/2}(Er_2{}^{3+}) \rightarrow {}^4I_{15/2}(Er1^{3+}) + {}^4I_{11/2}(Er_2{}^{3+})(\text{ET1})$$

Er^{3+} ions are excited from the $^4I_{11/2}$ state to the $^4F_{7/2}$ excited state by one of two probabilities, i.e., the excited state absorption (ESA1) and energy transfer from the $^4I_{11/2}$ state of a adjacent Er^{3+}, where two excited $^4I_{11/2}$ state Er^{3+} ions interact with each other and one ion is deexcited to the ground state $^4I_{15/2}$ and the other is excited to $^4F_{7/2}$ state. And of the Er^{3+} ions excited to the $^4F_{7/2}$ state, they mostly relax to the lower $^2H_{11/2}$ and $^4S_{3/2}$ states by multiphonon nonradiative process. The process can be described as [40]:

$$^4I_{11/2}(Er^{3+}) + h\nu(979\,\text{nm}) \rightarrow {}^4F_{7/2}(Er^{3+})(\text{ESA1})$$

$$^2I_{11/2}(Er1^{3+}) + {}^4I_{11/2}(Er^{3+}) \rightarrow {}^4I_{15/2}(Er^{3+}) + {}^4F_{7/2}(Er^{3+})(\text{ET2})$$

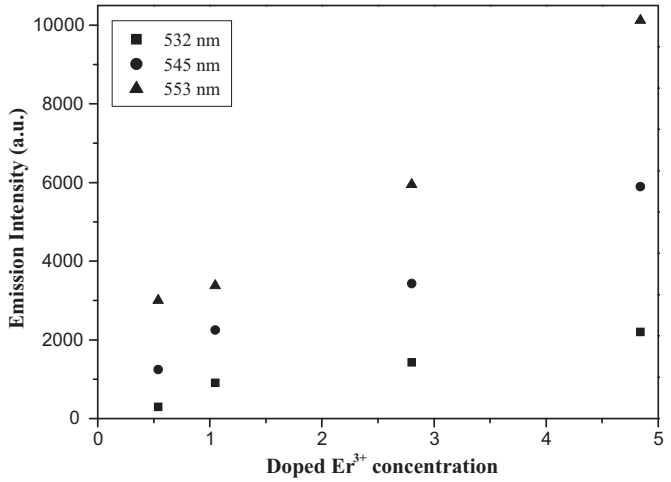

Fig. 7. Upconversion emission spectra of Er^{3+}:LiGd$(MoO_4)_2$ crystal with different Er^{3+} concentrations for π-polarization under 979 nm excitation at room temperature

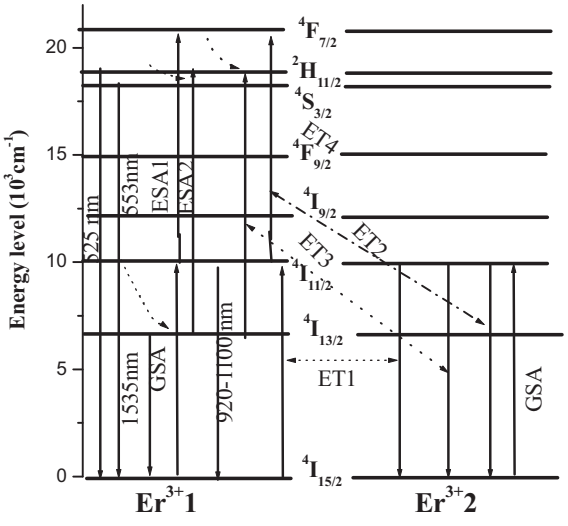

Fig. 9. Energy level diagram of Er^{3+} and the luminescence process by the 979 nm radiation LD pumping. The solid, dotted, and curly arrows represent the radiative, energy transfer, and multiphoton relaxation process, respectively.

$^4F_{7/2}(Er^{3+}) \rightarrow {}^4H_{11/2}, {}^4S_{3/2}(Er^{3+})$(the multi-phonon nonradiative process)

Since the lifetime of $^4I_{13/2}$ state is long (about 4.75 ms), Er^{3+} ions are also excited from the $^4I_{13/2}$ state to the $^4H_{11/2}$, $^4S_{3/2}$ states by ESA or energy transfer ET. The process is as following [40]:

$$^4I_{13/2}(Er^{3+}) + h\nu(979\,nm) \rightarrow {}^4H_{11/2}, {}^4S_{3/2}(Er^{3+})(ESA2)$$

$$^2I_{13/2}(Er^{3+}) + {}^4I_{11/2}(Er^{3+}) \rightarrow {}^4I_{15/2}(Er^{3+}) + {}^4H_{11/2}, {}^4S_{3/2}(Er^{3+})(ET3)$$

And of the Er^{3+} ions in the $^2H_{11/2}$,$^4S_{3/2}$ states transit to the $^4I_{15/2}$ ground state, producing the green emissions at 518–560 nm.

As well-known, the intensity of upconversion fluorescence caused by the energy transfer (ET) process is much stronger than that by the excited state absorption (ESA) process in the same condition [2], thereby, ET process is mainly responsible for the upconversion emission. As for ET process, the intensity of upconversion fluorescence depends on Er^{3+} concentration. When the Er^{3+} concentration in Er^{3+}:LiGd$(MoO_4)_2$ increases, the average instance between Er^{3+} ions shortens, the inter-ionic interaction enhances, thereby, the efficiency of energy exchange between Er^{3+} ions upgrades, more Er^{3+} ions are excited to $^4F_{7/2}$ and $^4S_{3/2}$ state, which gives rise to the acceleration of the population on the $^2H_{11/2}$,$^4S_{3/2}$ states, thus, the intensities of green light emission accordingly are enhanced.

4. Conclusions

The spectroscopic characterization and the upconversion emission mechanism of Er^{3+}:LiGd$(MoO_4)_2$ crystal grown by Czochralski technique were investigated. The Er^{3+}:LiGd$(MoO_4)_2$ crystal exhibits a large absorption cross section at 979 nm. The parameters of oscillator strengths, the spontaneous transition probabilities, the fluorescence branching ratios and radiative lifetimes were calculated based on Judd–Ofelt theory. The 1485–1650 nm emission band, corresponding to the $^4I_{13/2} \rightarrow {}^4I_{15/2}$ transition, exhibits large emission cross sections (0.63×10^{-20} and 0.48×10^{-20} cm^2 for π- and σ-polarization, respectively) and very large FWHM (around 110 nm). Green light emissions at 518-560 nm due to the $(^2H_{11/2}, {}^4S_{3/2}) \rightarrow {}^4I_{15/2}$ transition were observed at room temperature under 979 nm excitation. The emission cross sections were determined to be 4.37×10^{-20} and 1.93×10^{-20} cm^2 at 553 nm for π- and σ-polarization, respectively. The lifetime of $^4I_{13/2}$ and $(^2H_{11/2}, {}^4S_{3/2})$ level were measured to be 4.57 ms and 10.74 μs, respectively. The upconversion emission intensity became stronger with the increase of Er^{3+} concentration. The relationship between these upconversion intensities and the function of the pumping power shows that these emissions could be caused by two-photon processes. The upconversion emission mechanism is mainly involved with energy transfer. The investigated results reveal that the Er^{3+}:LiGd$(MoO_4)_2$ crystal may be regarded as a potential laser material.

Acknowledgments

This work was supported by the National Natural Science Foundation of China (No. 60808033), the Natural Science Foundation of Jiangxi Province (No. 2008GZW0012) and the Nature Science Foundation of Education Department of Anhui Province (No. KJ2010B203), respectively.

References

[1] A.A. Kaminski, Laser Crystals, Their Physics and Properties, vol. 14, 2nd Edition 246 Springer Ser. Opt. Sci., Springer Berlin, Heideberg, 1990.
[2] F. Auzel, Chem. Rev. 104 (2004) 139.
[3] S. Chandra, F.L. Deepak, J.B. Gruber, D.K. Sardar, J. Phys. Chem. C 114 (2010) 874.
[4] I.I. Leonidov, V.G. Zubkov, A.P. Tyutyunnik, N.V. Tarakina, L.L. Surat, O.V. Koryakova, E.G. Vovkotrub, J. Alloys Compd. 509 (2011) 1339.
[5] A. Amarnath Reddy, S. Surendra Babu, K. Pradeesh, C.J. Otton, G. Vijaya Prakash, J. Alloys Compd. 509 (2011) 4047.
[6] Ta-Ryeong Park, Solid State Commun. 150 (2010) 1378.
[7] R. Lisiecki, W. Ryba-Romanowski, E. Cavalli, M. Bettinelli, J. Lumin. 130 (2010) 131.
[8] Q. Dong, G.J. Zhao, D.H. Cao, J.Y. Chen, Y.C. Ding, J. Alloys Compd. 493 (2010) 661.
[9] X. Mateos, M.C. Pujol, F. Güell, R. Solé, Jna. Gavaldà, J. Massons, et al., Opt. Mater. 27 (2004) 475.
[10] X.Y. Huang, Z.B. Lin, L.Z. Zhang, G.F. Wang, Mater. Res. Innov. 12 (2008) 94.
[11] X.Y. Huang, Z.B. Lin, Z.S. Hu, G.F. Wang, J. Cryst. Growth 276 (2005) 177.
[12] Z.X. Cheng, S.J. Zhang, F. Song, H.C. Guo, J.R. Han, H.C. Chen, J. Phys. Chem. Solids 63 (2002) 2011.
[13] J.H. Huang, X.H. Gong, Y.J. Chen, Y.F. Lin, J.S. Liao, X.Y. Chen, et al., Appl. Phys. B 89 (2007) 73.
[14] X.A. Lu, Z.Y. You, J.F. Li, Z.J. Zhu, G.H. Jia, B.C. Wu, et al., J. Alloys Compd. 426 (2006) 352.
[15] G.M. Kuz'micheva, D.A. Lis, K.A. Subbotin, V.B. Rybakov, E.V. Zharikov, J. Cryst. Growth 75 (2005) e1835.
[16] X.Z. Li, Z.B. Lin, L.Z. Zhang, G.F. Wang, J. Cryst. Growth 293 (2006) 157.
[17] X.Z. Li, Z.B. Lin, L.Z. Zhang, G.F. Wang, J. Cryst. Growth 290 (2006) 670.
[18] D.K. Sardar, C.C. Russell III, R.M. Yow, J.B. Gruber, B. Zandi, E.P. Kokanyan, J. Appl. Phys. 95 (2004) 1180.
[19] X.Y. Huang, G.F. Wang, J. Alloys Compd. 475 (2009) 693.
[20] X.Y. Huang, Z.B. Lin, L.Z. Zhang, G.F. Wang, J. Cryst. Growth 306 (2007) 208.
[21] A.A. Kaminskii, A.A. Mayer, N.S. Nikonova, M.V. Provotorov, S.E. Sarkisov, Phys. Status Solidi (a) 16 (1972) K53.
[22] X.Y. Huang, G.F. Wang, J. Phys. D: Appl. Phys. 41 (2008) 225401.
[23] G.M. Kuz'micheva, V.B. Rytbakov, E.V. Zharikov, D.A. Lis, K.A. Subbotin, Rus. J. Inorg. Chem. 42 (2006) 303.
[24] B. Greenberg, Polytechnic Institute of rooklyn, New York, USA, ICDD Grant-in-Aid (1965).
[25] C. Cascales, M.D. Serrano, F. Esteban-Betegón, C. zaldo, R. Peters, K. Petermann, et al., Phys. Rev. B (74) (2006) 174114.
[26] G.M. Kuz'micheva, V.B. Rytbakov, V.L. Pantutin, E.V. Zharikov, K.A. Subbotin, Rus. J. Inorg. Chem. 55 (2010) 1448.
[27] G.M. Kuz'micheva, A.V. Eremin, V.B. Rytbakov, K.A. Subbotin, E.V. Zharikov, Rus. J. Inorg. Chem. 54 (2009) 854.
[28] E. Sani, A. Toncelli, M. Tonelli, D.A. Lis, E.V. Zharikov, K.A. Subbotin, et al., J. Appl. Phys. 97 (2005) 123531.
[29] B.R. Judd, Phys. Rev 127 (1962) 750.
[30] G.S. Ofelt, J. Chem. Phys. 37 (1962) 511.
[31] W.T. Carnall, P.R. Fields, K. Rajnak, J. Chem. Phys. 49 (1968) 4424.
[32] S.A. Payne, L.L. Chase, L.K. Smith, W.L. Kway, W.F. Krupke, IEEE J. Quantum Electron. 28 (1992) 2619.
[33] L. Wetenkamp, G.F. West, H. Tobben, J. Non-Cryst. Solids 140 (1992) 35.
[34] L. Fornasiero, E. Mix, V. Peters, K. Petermann, G. Huber, Ceram. Int. 26 (2000) 589.
[35] D.E. McCumber, Phys. Rev. 136 (1964) A954.
[36] B.F. Aull, H.P. Jenseen, IEEE J. Quantum Electron. 18 (1982) 925.
[37] T. Schweizer, T. Jensen, E. Heumann, G. Huber, Opt. Commun. 118 (1995) 557.
[38] B. Simondi-Teisseire, B. Viana, D. Vivien, A.M. Lejus, Phys. Stat. Solidi A 155 (1996) 249.
[39] N.A. Tolstik, A.E. Troshin, S.V. Kurilchik, V.E. Kisel, N.V. Kuleshov, V.N. Matrosov, et al., Appl. Phys. B 86 (2007) 275.
[40] A.J. Garcia-Adeva, R. Balda, J. Fernández, Ei Ei. Nyein, U. Hömmerich, Phys. Rev. B 72 (2005) 165116.